# Interaction-controlled transport in a two-dimensional massless-massive Dirac system: Transition from degenerate to nondegenerate regimes

A. D. Levin,[1] G. M Gusev,[1] F. G. G. Hernandez,[1] E. B. Olshanetsky,[2,3] V. M. Kovalev,[2,4,5] M. V. Entin,[2,3] and N. N. Mikhailov[2,3]

[1]*Departamento de Física dos Materias e Mecânica, Instituto de Física da Universidade de São Paulo, 135960-170 São Paulo, SP, Brazil*

[2]*Institute of Semiconductor Physics, Novosibirsk 630090, Russia*

[3]*Physics Department, Novosibirsk State University, Novosibirsk 630090, Russia*

[4]*Department of Semiconducting Devices and Microelectronics, Novosibirsk State Technical University, Novosibirsk 630073, Russia*

[5]*Abrikosov Center for Theoretical Physics, Moscow Institute of Physics and Technology, Dolgoprudny, 141701, Russia*

(Received 12 January 2024; revised 20 March 2024; accepted 2 April 2024; published 3 May 2024)

The resistivity of two-dimensional (2D) metals generally exhibits insensitivity to electron-electron scattering. However, it is worth noting that Galilean invariance may not hold true in systems characterized by a spectrum containing multiple electronic branches or in scenarios involving electron-hole plasma. In the context of this paper, we focus on 2D electrons confined within a triple quantum well (TQW) based on HgTe. This system displays a coexistence of energy bands featuring both linear and paraboliclike spectra at low energy and, therefore, lacks the Galilean invariance. This paper employs a combined theoretical and experimental approach to investigate the transport properties of this two-component system across various regimes. By manipulating carrier density and temperature, we tune our system from a fully degenerate regime, where resistance follows a temperature-dependent behavior proportional to $T^2$ to a regime where both types of electrons adhere to Boltzmann statistics. In the nondegenerate regime, electron interactions lead to resistance that is weakly dependent on temperature. Notably, our experimental observations closely align with the theoretical predictions derived in this paper. In this paper, we establish the HgTe-based TQW as a promising platform for exploring different interaction-dominant scenarios for the massless-massive Dirac system.

DOI: 10.1103/PhysRevResearch.6.023121

## I. INTRODUCTION

The impact of electron-electron scattering on the transport characteristics of various two-dimensional (2D) conductors, which do not adhere to Galilean invariance, has garnered significant attention over the years [1]. These studies typically focus on systems that involve two distinct types of charge carriers, characterized by differing charges or effective masses. The presence of two different charge carriers within the system, each with distinct mass, poses a challenge to the traditional concept of Galilean invariance. Consequently, the direct proportionality between the net current and the total particle momentum is no longer upheld [2–6]. Exploring the unique scenarios of strong friction between electrons and holes, particularly in degenerate 2D semimetals, has led to the observation of resistivity proportional to $T^2$ [7,8]. These phenomena have been validated in various experimental settings, most notably in HgTe quantum wells. Moreover, investigations into the nondegenerate regime have ventured into systems like single-layer and bilayer graphene, where thermally excited electron-hole pairs play a crucial role [9]. Recent advancements have also revealed electron-hole friction behavior in bilayer graphene systems, showcasing resistivity scaling as $T^2$ with spatially separated electrons and holes [10].

In a system comprising two subbands with significantly differing masses, it can be anticipated that the resistivity will exhibit a pronounced increase with rising temperature. This increase occurs due to the relationship between the resistivity limits at high and low temperatures, which is proportional to the effective mass ratio, as described in Ref. [1]. In such systems, the dominance of interactions in the transport process surpasses the Drude resistivity resulting from impurity or phonon scattering. The behavior of transport governed by interactions at elevated temperatures is characterized by the principles of hydrodynamics and is often referred to as electronic fluid behavior.

Another crucial question pertains to the investigation of interparticle collisions and hydrodynamic conductivity within a highly adjustable system. This system can be finetuned, transitioning from a nondegenerate Boltzmann regime to a degenerate Fermi-liquid regime.

As the understanding of electron hydrodynamics continues to unfold, it holds the promise of shedding light on the intricate interplay between particle-particle interactions, sample

geometry, and the distinct propertiesof charge carriers. This realm not only presents fundamental scientific inquiries but also offers potential applications in future electronic devices and technologies.

Previously, we offered a system that serves as a useful platform for studying transport dominated by interaction in 2D conductors [11]. This system is a 6.3 nm HgTe quantum well, representing the spectrum as a single-valley Dirac cone near the zero-energy state. However, it is important to note that, below theDirac zero-hole valleys with a minimum at a nonzero wave vector [11–16]. Consequently, when the chemical potential in the valence band reaches this lateral heavy-hole band, the Dirac holes experience strong scattering by heavy holes, and such scattering violations of Galilean invariance lead to a strong $T^2$ dependence of resistance. An interesting and important aspect of physics is explored in such conductors when heavy particles are partially degenerate: Dirac holes follow Fermi statistics, while heavy holes adhere to Boltzmann statistics. It is worth noting, however, that this system does not allow for a complete study of the transition from fully degenerate to nondegenerate regimes for all subsystems [11].

In this paper, we present an experimental situation that enables such an investigation. We have introduced the HgTe-based triple quantum well (TQW) as a convenient system featuring two subbands with both massless and massive Dirac fermions, specifically electrons. This stands in stark contrast with the singular HgTe well explored in a prior study [11], where the interaction between Dirac and heavy holes resulted in significant scattering. A TQW affords us the opportunity to investigate hydrodynamic conductivity across various regimes, including the strongly degenerate Fermi and nondegenerate Boltzmann regimes. Therefore, we illustrate that regardless of the sign, spectrum type, and other characteristicsof the carriers, including the confinement features of the multilayer system, electron-electron collisions exhibit unified properties and can emerge as the dominant mechanism in ultraclean systems. Consequently, TQWs emerge as a promising platform for exploring phenomena resulting from interactions. Notable instances encompass the violation of the Wiedemann-Franz law, as reported in Ref. [17], the prediction of giant magnetoresistance in Ref. [18], and quantum critical conductivity, detailed in Ref. [19], among other significant theoretical predictions.

## II. ELECTRON SPECTRUM IN A TRIPLE-WELL SYSTEM

HgTe-based quantum wells have garnered significant interest due to their capability to create unconventional 2D systems, such as 2D topological insulators [20–23]. Additionally, the behaviorof the spectrum is primarily determined by the thicknessof the well, leading to various phases characterized by insulating gaps, gapless regions, and inverted subbands [24–27]. Doublequantum wells (DQWs) and TQWs are multilayer systems comprising two or three quantum wells separated by a tunneling-transparent barrier. Theoretical investigations [28–30] haveproposed that the phase states within these structures are significantly altered when compared with the single quantum well scenario, which is supported by experimental evidence [31,32]. This alteration leads to a more

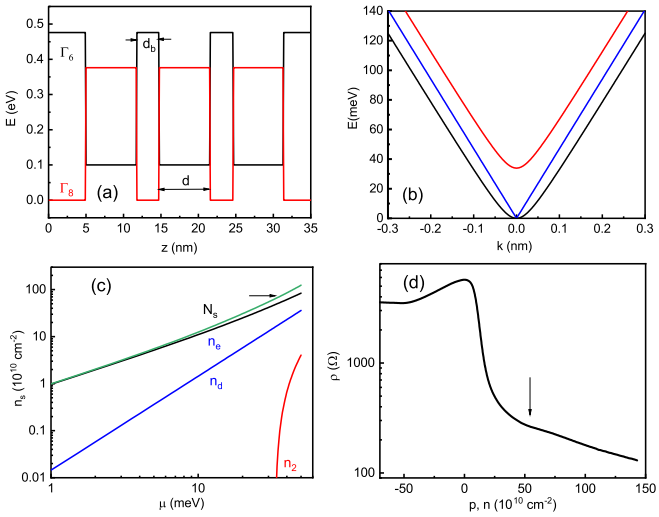


FIG. 1. (a) The conduction and valence band edges of the triple quantum well are schematically shown. The widths $d$ of the HgTe wells and the thickness $d_b$ of the $Hg_{1-x}Cd_xTe$ barriers ($x = 0.3$) are indicated. (b) The band structure of the triple HgTe well at $E > 0$ is calculated using the tight-binding model described in the text. The black and blue lines represent dispersion curves for massless and massive Dirac fermions. (c) The density of carriers is shown as a function of the chemical potential. $n_e$ and $n_d$ represent the densities of massive and massless electrons, $N_s$ is the total density. An arrow indicates the beginning of the $E^+$ subband populations. (d) The resistance of the 6.4 nm sample is plotted as a function of carrier density at $T = 4.2$ K.

complex phase landscape due to the additional degrees of freedom introduced by the increased number of 2D subbands and the hybridization induced by tunneling between them. Here, we illustrate that a HgTe-based TQW serves as a valuable platform for studying the influence of dominant interactions on transport behavior, primarily due to the unique characteristics of its spectrum.

Figure 1(a) depicts the band structure of HgTe TQWs with a thickness of $d_b = 3$ nm and a well width of $d = 6.7$ nm. The schematic representation displays the conduction and valence band edges of the TQW.

In Ref. [30], the authors haveconsidered the confinement characteristics of the subbands within HgTe/CdTe TQWs, along with their corresponding topological properties and edge state attributes. To accomplish this, they employ an effective 2D Hamiltonian for the HgTe-based triple-well system.

For single HgTe quantum wells, this is achieved by projecting the Hamiltonian onto its eigenstates at $k_{\text{II}} = 0$, leading to the well-established Bernevig-Hughes-Zhang (BHZ) model [26,27]. In contrast, for HgTe DQWs, two intriguing approaches are explored. First, like the derivation of the BHZ Hamiltonian, the authors of Ref. [28] haveprojected the overall Hamiltonian onto the eigenstates at $k_{\text{II}} = 0$ for the DQWs.

Alternatively, in Ref. [29], the authors haveprojected the total DQW Hamiltonian onto the subbands of the individual wells (left and right) and introduce tunneling parameters to account for the coupling between neighboring quantum wells.

In Ref. [30], the authors haveinvestigated the phase diagram of the HgTe triple well and transformed the

three-dimensional (3D) Kane Hamiltonian into an effective 2D 3BHZ model. This transformation enabled them to explore the edge state characteristics in each topological phase.

These findings reveal the existence of gapless phases, attributed to the slight hybridization of $H$-like states from different quantum wells. In these gapless phases, one or two pairs of edge states are present within the bulk. However, there is also a phase where all $E$-like and $H$-like subbands are inverted, leading to the formation of three sets of edge states within a bulk gap.

Moreover, for a triple well with a well width of $d = 6.7$ nm, the subbands $E_{01}$ and $H_{01}$ exhibit significant hybridization, resulting in nearly negligible mass for a linear Dirac subband. Meanwhile, the second subband maintains a $k$-parabolic spectrum with massive Dirac fermions at low energies. This effect has been substantiated through the measurement of Schubnikov–de Haas oscillations [30].

To obtain the analytical expression for the triple-energy Hamiltonian is

$$H = \begin{pmatrix} 0 & Ak & 0 & 0 & 0 & 0 \\ Ak & 0 & t & 0 & 0 & 0 \\ 0 & t & 0 & Ak & 0 & t \\ 0 & 0 & Ak & 0 & 0 & 0 \\ 0 & 0 & 0 & 0 & 0 & Ak \\ 0 & 0 & t & 0 & Ak & 0 \end{pmatrix}, \tag{1}$$

where $k$ is the 2D momentum operator, $A = \hbar v_F \approx 470$ meV nm, $v_F$ is the Fermi velocity of the single HgTe well, and the in-plane nearest-neighbor hopping is $t \approx 24$ meV.

One can see that the Hamiltonianin Eq.(1) leads to a combination of two linear bands and four massive bands:

$$\begin{aligned} E_s &= \pm\left[t^2 + v_F^2 k^2 + s\sqrt{t^4 + 2t^2 v_F^2 k^2}\right]^{1/2}, \\ s &= \pm 1 \\ E_0 &= \pm v_F k. \end{aligned} \tag{2}$$

In Fig. 1(b), we present the electronic segment of the spectrum. The Dirac-like spectrum is represented by the blue lines, whereas the massive Dirac subbands are denoted by the black and red lines. It is worth noting that the simplified tight-binding model provides a good fit for the electronic branches, consistent with those obtained using the Kane model [30]. However, there is a notable difference for the hole segments of the spectrum. Therefore, in this paper, we concentrate solely on the electronic spectrum.

It is noteworthy that, in symmetric HgTe TQWs, the transition from a gapless to a gapped phase can be achieved by disrupting the inversion symmetry of the wells through the application of a transverse electric field, either from asymmetric doping or external gate bias [29,31]. This process can induce a small gap in the energy spectrum, reminiscent of phenomena seen in bilayer and trilayer graphene. The ability to manipulate this gap with an external field is fascinating, offering avenues to modulate edge state transport within HgTe double- and triple-well configurations. As we will show in the next paragraph, we detected a minimal gap in our structures, indicated by activation resistance behavior, on the order of $\sim$1 meV. However, it is critical to underline that this gap, while present, is minuscule relative to other system parameters and does not notably affect the spectrum as outlined by Eq. (1). Our investigation primarily concentrated on the conduction band, which is essentially unaffected by such a negligible gap.

Due to the Dirac-like nature of the Hamiltonian, the behavior of the density of states significantly deviates from that of conventional 2D systems. In the spectrum of subbands denoted by $E_s$, we observe a nearly parabolic shape, with particles exhibiting significant mass only in the vicinity of $k \approx 0$. As energy levels increase, the spectrum also transitions to a linear regime. This leads to a linear dependence of the density of states on energy and a nonmonotonic change in the chemical potential with respect to gate voltage.

In Fig. 1(c), the density of 2D carriers, distributed across different subbands, is depicted as a function of the chemical potential $\mu$. Notably, it is evident that the density of carriers in the massive Dirac branch surpasses that of the massless carriers. Furthermore, beyond an energy threshold of 35 meV, the second subband of the massive Dirac fermions starts to become occupied.

The presence of various electronic branches leads to the breakdown of Galilean invariance and a noteworthy increase in the impact of scattering between these branches on electronic transport.

## III. EXPERIMENTAL RESULTS

We fabricated TQWs using HgTe/$Cd_xHg_{1-x}$Te material with a [013] surface orientation. The wells had equal widths, with $d_0$ measuring 6.7 nm and a barrier thickness of $t$ set at 3 nm. The layer thickness was monitored during molecular beam epitaxy (MBE) growth via ellipsometry, achieving an accuracy within $\pm 0.3$ nm.

The devices employed in this paper were multiterminal bars featuring three consecutive segments, each 3.2 μm wide, with varying lengths of 2, 8, and 32 μm. These devices were equipped with nine contacts. The contacts were created by indium bonding to the surface of the contact pads, which were precisely defined using lithography. Given the relatively low-growth temperature ($\sim$180 °C), the temperature during the contact fabrication process remained low as well. Indium diffused vertically downward on each contact pad, establishing an ohmic connection across all three quantum wells, with contact resistance falling within the 10–50 kΩ range. Throughout the AC measurements, we consistently verified that the reactive component of impedance did not exceed 5% of the total impedance, confirming the effectiveness of the ohmic contacts. Furthermore, the current-voltage ($I$-$V$) characteristics exhibited ohmic behavior at low voltages. A 200 nm $SiO_2$ dielectric layer was deposited onto the sample surface, subsequently covered by a TiAu gate. The density variation with gate voltage was estimated to be $\sim 0.9 \times 10^{11}$ cm$^{-2}$/V, derived from the dielectric thickness and Hall measurements, as previously reported in studies employing similar devices. Two samples, denoted as A and B, were studied. The samples were created from a uniform substrate and were subject to identical growth conditions. It is important to emphasize that these samples are of mesoscopic dimensions and, as such, are expected to display all characteristics inherent to mesoscopic physics.

TABLE I. Some of the typical parameters of the electron system in HgTe TQW at $T = 4.2$ K.

| Sample | $d$ (nm) | $V_{\mathrm{CNP}}$ (V) | $\rho_{\max}(h/e^2)$ | $\mu_e$ (V/cm$^2$s) |
|---|---|---|---|---|
| A | 6.7 | −3.6 | 0.22 | 33.600 |
| B | 6.7 | −6.7 | 0.2 | 39.600 |

Figure 1(d) illustrates the variation of resistivity with charge density for sample A at a temperature of 4.2 K. The resistance shows a prominent peak centered at the charge neutrality point(CNP), which corresponds to the zero-energy point. This behavior is a characteristic feature of both gapless and gapped HgTe single-well devices [16,31]. The maximum electron density corresponds to a Fermi energy value of ∼150 meV, as depicted in Fig. 1(c). As the chemical potential approaches the range of 30–40 meV, the second subband associated with massive Dirac fermions begins to be occupied. This is evident from a small feature in the resistivity, as indicated by the arrow in Fig. 1(d). Table I presents the key parameters of the gapless HgT quantum well employed in this paper. These parameters include the well width ($d$), the gate voltage associated with the Dirac point position ($V_{\mathrm{CNP}}$), the resistivity ($\rho$ value) at the CNP, and the electron mobility ($\mu_e$) calculated as $1/\rho N_s$, where the total electron density ($N_s$) is set at $2 \times 10^{11}$ cm$^{-2}$.

Figure 2 illustrates the variation in resistance with respect to gate voltage across a wide range of temperatures. The plot reveals a notable increase in resistance as temperature rises, with one notable exception: In the voltage region close to the CNP ($-3V < V_g - V_{\mathrm{CNP}} < 0V$), the resistance exhibits insulating behavior characterized by a very slight activation gap in the range of 0.5–0.8 meV. The reduction in resistance as temperature increases can be attributed to potential fluctuations, which may lead to the creation of small semimetallic insulating regions or residual gaps. It is important to acknowledge that even a small gap has the potential to alter the energy spectrum described by Eq. (2). However, for the sake of simplicity, we have omitted such modifications in our straightforward model.

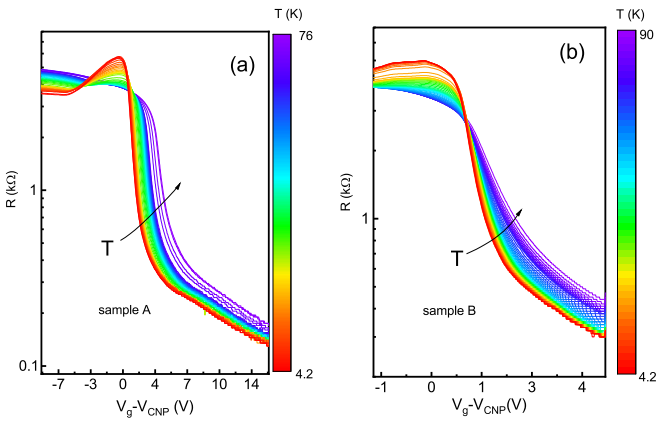


FIG. 2. Resistance as a function of the gate voltage at different temperatures for two HgTe triple quantum wells.

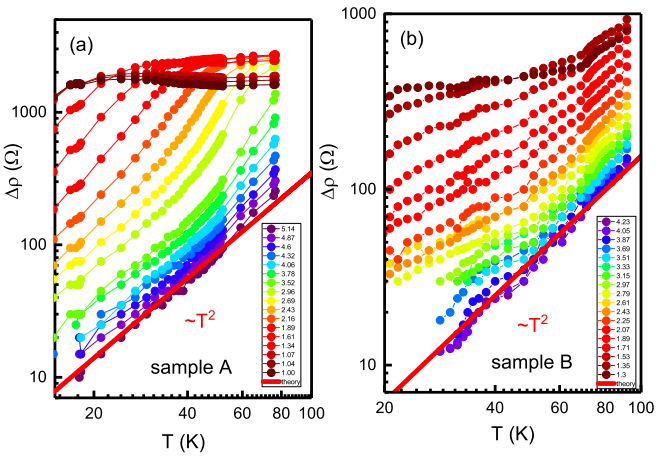


FIG. 3. Excess resistivity $\Delta\rho(T) = \rho(T) - \rho(T = 4.2\,\mathrm{K})$ as a function of the temperature for various densities for samples (a) A and (b) B. The red lines show $T^2$ dependence. The values of the densities are given in $10^{11}$ cm$^{-2}$.

To further investigate the temperature-dependent behavior of resistance (or resistivity), we calculate the excess resistivity, denoted as $\Delta\rho(T) = \rho(T) - \rho(T = 4.2\,\mathrm{K})$.

Subsequently, in Fig. 3, we present the excess resistivity for different electron densities across a broad temperature range, for samples A and B. It is evident that the temperature dependence evolves, adhering closely to a $T^2$ relationship at high electron densities, while exhibiting weak temperature dependence near the CNP. It is noteworthy that, in the intermediate density regime, the temperature dependence displays a somewhat more complex behavior. At low temperatures, the dependence in sample A resembles a quadratic function, whereas at higher temperatures, the power becomes significantly more pronounced. In contrast, for sample B, the temperature dependence remains quadratic at high temperatures, but the power is diminished at lower temperatures. At low densities, sample A exhibits an almost plateaulike behavior at high temperatures, while sample B demonstrates an increase in excess resistivity. We believe that sample B displays greater levels of disorder and inhomogeneity and that contributions from regions of higher density become critical at elevated temperatures. At high densities, the experimental curve follows a quadratic dependence with a difference in the order of amplitude for both samples. In the following discussion, we focus on the high-density dependencies for a comparison with theoretical predictions.

Figures 4 anpoints at low temperatures exhibit dispersion due to their limited precision. In sample B, we also observed a more rapid growth of excess resistivity with increasing temperature, which deviated from the $T^2$ trend, possibly owing to the broadening of the distribution function. We will delve further into the Boltzmann statistical regime in the subsequent section.

The distinct resistance dependence of $T^2$ serves as an unambiguous indicator of electron-electron scattering, as opposed to phonon scattering, which would lead to a linear, rather than quadratic, temperature dependence, as discussed in Ref. [33]. While it is a well-established fact that electron-electron interactions do not influence the resistivity of a

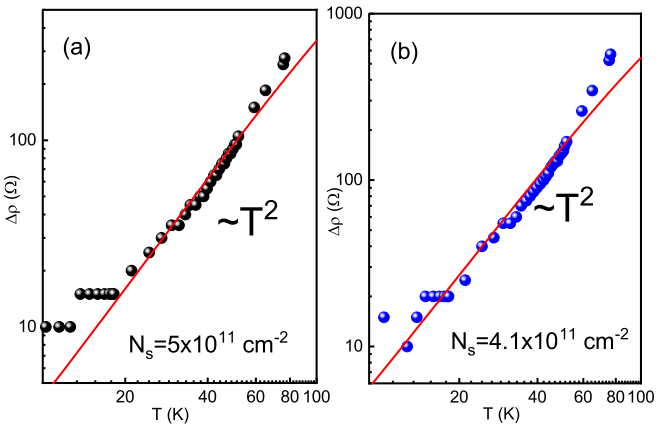


FIG. 4. Excess resistivity $\Delta\rho(T) = \rho(T) - \rho(T = 4.2\,\mathrm{K})$ as a function of the temperature for two different densities for sample A. The total density is (a) $N_s = 5 \times 10^{11}\,\mathrm{cm}^{-2}$and (b) $N_s = 4.1 \times 10^{11}\,\mathrm{cm}^{-2}$. Circles represent the experimental data, and the red lines represent the theory of interparticle scattering between the fully degenerate massless and massive electrons.

Galilean-invariant Fermi liquid, there are specific scenarios where a conductivity proportional to $T^{-2}$ can be observed, as detailed in Ref. [1]. Such scenarios include the presence of spin-orbit interactions or the involvement of multiple subbands, as discussed in Refs. [1–5,34].

Notably, Fig. 2 reveals an extraordinary observation: The resistivity ratio between high and low temperatures $\rho(T = 70\,\mathrm{K})/\rho(T = 4.2\,\mathrm{K})$, surpasses the 4–5 limit, signifying that $\Delta\rho$ is significantly greater than $\rho(T = 4.2\,\mathrm{K})$ at elevated temperatures. This striking departure from more conventional scenarios, where resistance is predominantly influenced by disorder or phonon scattering, underscores the critical role of particle-particle collisions in this context. These collisions have a pronounced impact, far exceeding that of impurity-related scattering. This observation validates the HgTe-based triple well as a promising experimental platform for investigating transport phenomena dominated by interactions, opening the door to the exploration of nontrivial effects, such as violations of the Wiedemann-Franz law [17], anomalous Coulomb drag [35], and many others (for areview, see Ref. [36]).

## IV. COMPARISON OF THEORY WITH EXPERIMENT

In the following discussion, we examine a straightforward hydrodynamic model with two subbands, wherein electron-electron scattering is characterized by a concept of mutual friction. The conductivity is determined through an equation of motion for the electron featuring Dirac dispersion and massive electrons:

$$-\frac{v_d - v_e}{\tau_{de}} - \frac{v_d}{\tau_d} + \frac{qE}{m_d} = 0, \tag{3}$$

$$-\frac{v_e - v_d}{\tau_{ed}} - \frac{v_e}{\tau_e} + \frac{qE}{m_e} = 0, \tag{4}$$

where variables $v_d$ and $v_e$ are drift velocities of the massless (Dirac) and massive electrons. The solutions of these equations have been performed elsewhere [8,10,11]. The expression for conductivity can be obtained with some modifications, and it is given by

$$\sigma = q^2 \frac{n_d n_e \left[\tau_d\left(\tau_e + \tau_{\mathrm{int}}\right)\left(2 + \frac{n_d}{n_e}\right) + \tau_e(\tau_d + \tau_{\mathrm{int}})\frac{n_e}{n_d} + \tau_{\mathrm{int}}\left(\frac{m_e}{m_d}\tau_d - \frac{m_d}{m_e}\tau_e\right)\right]}{m_e n_e(\tau_d + \tau_{\mathrm{int}}) + m_d n_d(\tau_e + \tau_{\mathrm{int}})}. \tag{5}$$

We introduce the following variables: $n_e$ and $n_d$, representing the densities of massive and massless electrons, respectively, and $\tau_e$ and $\tau_d$ as their respective scattering times, due to impurities and static defects. Furthermore, we define $N_s$ as the total electron density. In addition, $q$ is the elementary charge, $m_e = \hbar^2 k \frac{dk}{dE_s}$ is the heavy electron effective mass, $m_d = \mu/v_F^2$ is the Dirac electron effective mass, $\tau_{ed(de)}$ is the collision time with theheavy (Dirac) electron per Dirac (heavy) electron. We also introduce $1/\tau_{\mathrm{int}} = 1/\tau_{de} + 1/\tau_{ed}$. The equation, considering the constraint that interactions between massive and massless Dirac electrons conserve the overall momentum density, is $n_d m_d \tau_{de} = n_e m_e \tau_{ed}$. Hence, the term in Eq. (5) that remains temperatureindependent is anticipated to be primarily governed by interface roughness and impurity scattering, as discussed in Ref. [33]. Conversely, the temperature-dependent component of resistivity can be attributed to electron-electron (e-e) friction within the non-Galilean-invariant massive-massless Dirac liquid.

An insightful analysis would involve examining the limits of $T = 0$ and $T = \infty$, especially in cases where the effective masses differ significantly. The effective scattering timeof the Dirac hole can be approximated using the relation $m_d = \mu/v_F^2 \approx 0.006 m_0$, with $\mu \approx 16\,\mathrm{meV}$. At $T \to 0$, both bands contribute to the total conductivity dominated by the Dirac holes:

$$\sigma(T = 0) = \frac{q^2 n_d v^2 \tau_d}{\mu} = \frac{q^2 n_d \tau_d}{m_d}. \tag{6}$$

At $T = \infty$, the conductivity becomes temperature independent and saturates at a value approximately determined by the conductivity of the heavy:

$$\sigma(T = \infty) = \frac{q^2 (n_d + n_e)^2 \tau_e}{m_e n_e}. \tag{7}$$

In our case, $n_e \gg n_d$, the ratio of the resistivities at both temperature limits is determined by

$$\frac{\rho(T = \infty)}{\rho(T = 0)} = \frac{m_e n_d \tau_d}{m_d n_e \tau_e}. \tag{8}$$

When $n_e \tau_e \sim n_d \tau_d$, the ratio of the resistivities at these temperature extremes is predominantly influenced by the effective mass ratio (for Fermi energy $E_F = 5\,\mathrm{meV}$) [1]:

$$\frac{\rho(T = \infty)}{\rho(T = 0)} \approx \frac{m_e}{m_d} \approx 4.4. \tag{9}$$

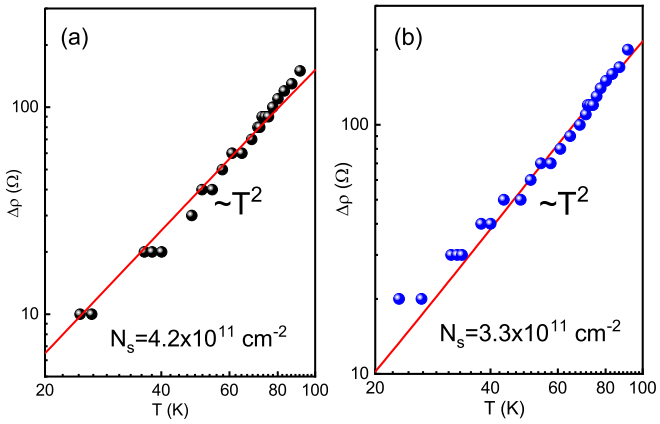


FIG. 5. Excess resistivity $\Delta\rho(T) = \rho(T) - \rho(T = 4.2\,\mathrm{K})$ as a function of the temperature for two different densities for sample B. The total density is (a) $N_s = 4.2 \times 10^{11}\,\mathrm{cm}^{-2}$and (b) $N_s = 3.3 \times 10^{11}\,\mathrm{cm}^{-2}$. Circles represents the experimental data, and the red lines represent the theory of interparticle scattering between the fully degenerate massless and massive electrons.

Hence, it is reasonable to anticipate that, in the optimal system where electron-electron interactions govern transport, there will be energy branches characterized by distinct effective masses. The gapless HgTe system stands out as a highly promising platform for conducting this type of research.

In a regime of full degeneracy, where both types of electrons adhere to Fermi statistics, an expression for particle-particle collisions has been derived, with slight modifications to account for the difference in their energy spectra [11]:

$$\frac{1}{\tau_{de}} = \alpha \frac{m_e (kT)^2 U_0^2}{3\pi\hbar^5 v v_F} \equiv \frac{1}{\tau_0} \sim T^2, \tag{10}$$

$$\frac{1}{\tau_{ed}} = \frac{1}{\tau_0} \frac{\mu}{m_e v_F^2} \frac{n_d}{n_e} \sim T^2, \tag{11}$$

where $U_0 = \frac{2\pi e^2}{\epsilon q_s}$, $q_s = \frac{me^2}{\varepsilon\hbar^2}$, $\epsilon$ is the dielectric constant of the material, $v$ is Fermi velocity of the massive particle, andpref-actor $\alpha$ represents a numerical coefficient that varies based on the specifics of the Coulomb interactions. Note that $1/\tau_{ed} \ll 1/\tau_{de}$, and conventional $T^2$ behavior for $1/\tau_{\mathrm{int}} \sim 1/\tau_{de}$, char-acteristic of a particle with parabolic dispersion, becomes evident.

Remember that, in the case of finite temperature, the elec-tron density can be found from the equation:

$$n_{d,e} = \int_0^\infty D_\varepsilon^{d,e} \left[1 + \exp\left(\frac{\varepsilon - \mu}{kT}\right)\right]^{-1} d\varepsilon, \tag{12}$$

where $D_\varepsilon^{d,e}$ is the density of the states of the Dirac and massive electrons, respectively. It is essential to emphasize that, even though the density in each subband strongly re-lies on the temperature at high $T$ or in the nondegenerate regime, the total density is constrained by the gate voltage, expressed as $n_e + n_d = N_s \sim V_g$. As a result, the chemical potential can be parametrically determined. To compare with the theoretical framework, we performed a fitting analysis on the temperature-dependent data, as illustrated in Figs. 4 and 5.

TABLE II. Fitting parameters in Eqs. (5) and (10) for 2 samples.

| Sample | $E_F$ (meV) | $N_s$ $10^{11}$ ($\mathrm{cm}^{-2}$) | $\tau_e$ $10^{-13}$ (s) | $\tau_d$ $10^{-13}$ (s) | $n_e$ $10^{11}$ ($\mathrm{cm}^{-2}$) | $n_d$ $10^{11}$ ($\mathrm{cm}^{-2}$) | $\alpha$ |
|---|---|---|---|---|---|---|---|
| A | 33.8 | 5 | 0.31 | 4.7 | 3.3 | 1.7 | 0.5 |
| A | 30.4 | 4.2 | 0.3 | 4.6 | 2.8 | 1.3 | 0.7 |
| B | 30.7 | 4.2 | 0.29 | 4.3 | 2.8 | 1.3 | 0.17 |
| B | 26.5 | 3.3 | 0.41 | 5 | 2.3 | 1 | 0.2 |

This analysis involved a single adjustable parameter denoted as $\alpha$, which accounts for the interaction strength between the Dirac and massive holes, as outlined in Eqs. (5)–(11). The scattering parameters, referred to as $\tau_{e(d)}$, play a predominant role in determining resistivity at lower temperatures. Impor-tantly, varying these parameters within a reasonable range does not impact the friction coefficient, which is the primary driver of temperature-dependent resistivity. In Figs. 4 and 5, we present the theoretical dependencies of resistivity excess for various total density values. Notably, the experimental data closely align with the expected dependence $\Delta\rho(T) \sim T^2$ for the parameters specified in Table II.

It is evident that the prefactor $\alpha$, introduced as an ad-justable parameter reflecting the difference between the actual Coulomb potential and the contact interaction potential, is close to unity and exhibits a tendency to increase as the particle density decreases. It is worth noting, however, that the corresponding prefactor for sample B is smaller than that of sample A. It is important to note that both samples exhibit a resistivity pattern consistent with the $T^2$ law within one order of magnitude.

## V. COMPARISON OF THE THEORY WITH EXPERIMENT IN NONDEGENERATE REGIME

At low densities and moderately high temperatures, both massive and massless Dirac electrons start adhering to Boltzmann statistics. In this regime, an expression for electron-electron collisions has been formulated, incorporat-ing minor adjustments to accommodate variations in their energy spectra:

$$\frac{1}{\tau_{de}^*} = \beta \frac{\sqrt{\pi}}{6} \frac{n_e}{(kT)^3} \frac{v_T m_e^4 v_F^5}{\hbar^3} U_0^2 \mathfrak{J}_1 \sim T^{-1/2} \mathfrak{J}_1(T), \tag{13}$$

$$\frac{1}{\tau_{ed}^*} = \beta \frac{\sqrt{\pi}}{4} \frac{n_d}{(kT)^2} \frac{v_T m_e^3 v_F^3}{\hbar^3} U_0^2 \mathfrak{J}_2 \sim T^{1/2} \mathfrak{J}_2(T), \tag{14}$$

where $U_0 = \frac{2\pi e^2}{\epsilon q_T}$, $q_T = \frac{2\pi e^2 n_e}{\varepsilon(kT)}$, $\epsilon$ is the dielectric constant of the material, $v_F$ is theFermi velocity of massless Dirac particles, and$v_T = \sqrt{\frac{2kT}{m_e}}$ is velocity of massive particles. The prefactor denoted by $\beta$ corresponds to a numerical coeffi-cient that depends on the details of the Coulomb interactions.

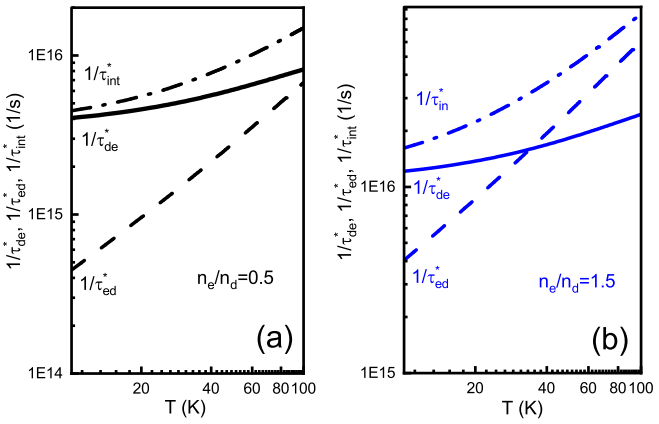


FIG. 6. Temperature dependence of the relaxation rate for different density ratios $n_e/n_d$. Solid lines are computed using Eqs. (13) and (15) [$1/\tau^*_{de}$, dashes are computed using Eqs. (14) and (16) ($1/\tau^*_{ed}$)], dot-dashes represent $1/\tau^*_{\rm int}$. Total density $N_s = 3 \times 10^{10}\,{\rm cm}^{-2}$, (a) ratio $n_e/n_d = 0.5$ (black lines) and (b) $n_e/n_d = 1.5$ (blue lines).

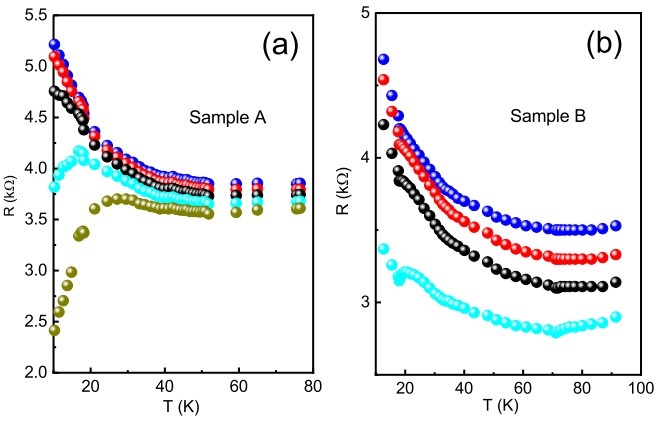


FIG. 7. (a) Resistivity $\rho(T)$ as a function of temperature for different densities for sample A. The total density is $N_s \approx 0$ (charge neutrality point, blue), $N_s \approx 3 \times 10^{10}\,{\rm cm}^{-2}$ (red), $N_s \approx 6.1 \times 10^{10}\,{\rm cm}^{-2}$ (black), $N_s \approx 8 \times 10^{10}\,{\rm cm}^{-2}$ (cyan), and $N_s \approx 10 \times 10^{10}\,{\rm cm}^{-2}$ (dark yellow). (b) Resistivity $\rho(T)$ as a function of temperature for different densities for sample B. The total density is $N_s \approx 0$ (charge neutrality point, blue), $N_s \approx 3 \times 10^{10}\,{\rm cm}^{-2}$ (red), $N_s \approx 6.1 \times 10^{10}\,{\rm cm}^{-2}$ (black), and $N_s \approx 8 \times 10^{10}\,{\rm cm}^{-2}$ (cyan).

Integrals $\mathfrak{J}_{1,2}$ are represented by the following expressions:

$$\mathfrak{J}_1 = \int_0^\infty y^2 dy \int_{-1}^{1} \sqrt{1-x^2} \exp\left[-\frac{m_e v_F^2}{2kT}\left(x+\frac{y}{2}\right)^2\right] dx, \quad (15)$$

$$\mathfrak{J}_2 = \int_0^\infty y^2 dy \int_{-1}^{1} \frac{\exp\left[-\frac{m_e v_F^2}{2kT}\left(x+\frac{y}{2}\right)^2\right]}{\sqrt{1-x^2}} dx. \quad (16)$$

Figure 6 depicts the correlation between the relaxation rates $1/\tau_{de}$ and $1/\tau_{ed}$ and temperature, represented by the blue and black lines. The computations employ Eqs. (13) and (14) with the parameter $\beta$ set to 1. Due to the integrals $\mathfrak{J}_{1,2}$ behaving approximately like power functions of $T^\delta$ with $\delta \approx 0.5$, the relaxation rates exhibit distinct temperature dependencies. Specifically, the rate $1/\tau_{de}$ is a weakly temperature-dependent function, while the collision rate $1/\tau_{ed}$ follows a quasilinear $T$ dependence.

The relationship between rates $1/\tau_{de}$ and $1/\tau_{ed}$ depends on the ratio $n_e/n_d$ and the temperature interval. Notably, over a wide temperature range, the interaction rate maintains the relationship $1/\tau_{de} > 1/\tau_{ed}$ for $n_e/n_d = 1.5$. Moreover, the relaxation rate $1/\tau_{de}$ surpasses $1/\tau_{de}$ at temperatures exceeding 35 K for the inverse relation $n_e/n_d = 1.5$. It is essential to note that interactions between massive and massless Dirac electrons conserve the overall momentum density, and the total relaxation rate involved in the transport coefficient is given by $1/\tau^*_{\rm int} = 1/\tau^*_{de} + 1/\tau^*_{ed}$. The temperature dependence of the relaxation rate $1/\tau^*_{\rm int}(T)$ describes an intermediate power with a temperature-dependent exponent index.

In Fig. 1(c), the chemical potential exhibits a range of variation from 1 to 3 meV for total electron densities in the order of $1 \times 10^{10}$ to $3 \times 10^{10}\,{\rm cm}^{-2}$. Within this density range, we can assert that both massive and massless Dirac electrons adhere to Boltzmann statistics for temperatures between 10 and 100 K.

Figures 7(a) and 7(b) illustrate the temperature dependence of resistance in the vicinity of the CNP for low electron densities. It is evident that resistance decreases as the temperature increases near the CNP. This trend is attributed to the presence of a small gap in the spectrum, approximately $\Delta \sim 1$ meV, leading to an activation law $R \sim \exp(\Delta/2kT)$ for the resistance, as indicated in Ref. [30]. Additionally, this behavior is justified by the quantization of resistance and nonlocal resistance resulting from the helical edge states, confirming the topological insulator nature of the triple HgTe-based quantum well, as demonstrated in our previous publications [30]. Furthermore, it is crucial to note that, although the involvement of helical edge states is significant, especially when the chemical potential resides within the gap, their contribution becomes negligible when $\mu$ is shifted to the conductivity band, and the edge states become heavily intertwined with the bulk conductivity.

Beyond the CNP, we observe weakly temperature-independent resistance, as depicted in Figs. 3(a) and 3(b) and more comprehensively in Figs. 7(a) and 7(b). Notably, a strong temperature dependence of resistance is discernible far from the CNP, where the resistance increases by more than an order of magnitude with rising temperature. This observation underscores distinct transport regimes in the regions near and far from the CNP—specifically, for low densities where a nondegenerate system can be anticipated and at high densities where the system becomes degenerate across the entire temperature range.

To assess the agreement of our results with theory in the nondegenerate regime, we computed the resistivity using Eqs. (5) and (13)–(16). Figure 8 illustrates these calculations for a total density $N_s = 3 \times 10^{10}\,{\rm cm}^{-2}$ and various density ratios $n_d/n_e (T = 4.2\,{\rm K})$. Interestingly, there is a small (∼2%) reduction in resistance with increasing temperature. This finding may seem surprising given the distinct growth observed in the scattering time $1/\tau^*_{\rm int}(T)$ (see Fig. 6). It is essential to note, however, that in the Boltzmann regime, several parameters are expected to exhibit temperature dependence.

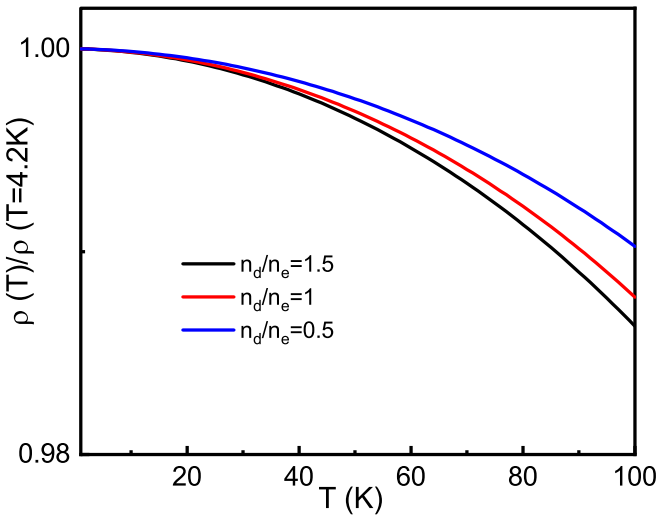


FIG. 8. (a) The resistivity ratio$\rho(T)/\rho(T = 4.2\,\mathrm{K})$ as a function of temperature for different parameters calculated from Eqs. (5), (13), and (14). Total density $N_s = 3 \times 10^{10}\,\mathrm{cm}^{-2}$, the ratio $\tau_e/\tau_d = 5$, $\tau_d = 0.4 \times 10^{-12}$ s, andthe ratio $n_d/n_e(T = 4.2\,\mathrm{K}) = 1.5$ (black), 1 (red), and 0.5 (blue). Parameter $\beta = 1$.

Primarily, the densities of massive and massless electrons strongly depend on temperature in the nondegenerate regime [see Eq. (12)]. Despite this, as previously mentioned, the total density remains fixed by the external gate voltage, suggesting a substantial redistribution of charge carriers as temperature increases. Additionally, the effective mass exhibits strong temperature dependence, significantly contributing to the temperature-dependent resistivity. These temperature-dependent parameters counterbalance the increase in the relaxation rate $1/\tau^*_{\mathrm{int}}(T)$ and ultimately result in only a weakly temperature-dependent resistance. This effect bears some similarity to the situation in graphene, where the nondegenerate limit has been explored in single-layer and bilayer graphene, with electron-hole pairs being thermally excited [9,37]. In these cases, the electron-hole collision rate is expected to be proportional to $T$, leading to temperature-independent conductivity.

It is important to acknowledge that our model, while informative, is overly simplistic for capturing the intricate details observed in the experimental data presented in Figs. 7(a) and 7(b), particularly in terms of exact evolution of the resistance with $T$. Achieving a more accurate agreement with the experimental results, especially with Eq. (5), necessitates a precise understanding of the behavior of the density of states within the gap.

Additionally, our tight-binding model, though useful, is too rudimentary to accurately characterize parameters in the vicinity of the CNP, where potential disorder may also contribute to smoothing effects. Consequently, it becomes evident that the weak temperature dependence observed in the experiments near the CNP aligns with our theoretical model to a certain extent. However, it is crucial to recognize the limitations of our model and acknowledge the need for more sophisticated approaches to capture the nuances exhibited by the experimental data.

## VI. CONCLUSION

In summary, in this paper, we focused on the temperature-dependent resistivity in a triple HgTe quantum well that accommodates two branches of fermions, one with massive and the other with massless Dirac characteristics. We observed quadratic temperature dependencies resulting from interactions between the Dirac fermions and massive electrons in the fully degenerate regime. In contrast, when both type of electrons adhered to Boltzmann statistics, resistivity remained weakly temperature dependent.

Our findings validate that the presented model comprehensively describes the conductivity of the TQW across a broad spectrum of temperatures and carrier densities. In our ultra-clean samples, electron-electron scattering takes precedence, exerting a significantly more notable impact than impurity scattering. It also demonstrates the unified nature of hydrodynamic transport across different systems, irrespective of the sign and spectrum typeof the carriers.

## ACKNOWLEDGMENTS

This paper is supported by FAPESP (São Paulo Research Foundation) Grants No. 2019/16736-2 and No. 2021/12470-8, National Council for Scientific and Technological Development, and by the Ministry of Science and Higher Education of the Russian Federation and Foundation for the Advancement of Theoretical Physics and Mathematics BASIS.

[1] H. K. Pal, V. I. Yudson, and D. L. Maslov, Resistivity of non-invariant Fermi- and non-Fermi liquids, Lith. J. Phys. **52**, 142 (2012).

[2] K. E. Nagaev and A. A. Manoshin, Electron-electron scattering and transport properties of spin-orbit coupled electron gas, Phys. Rev. B **102**, 155411 (2020).

[3] K. E. Nagaev, Electron-electron scattering and conductivity of disordered systems with a Galilean-invariant spectrum, Phys. Rev. B **106**, 085411 (2022)

[4] S. S. Murzin, S. I. Dorozhkin, G. Landwehr, and A. C. Gossard, Effect of hole-hole scattering on the conductivity of the two-component 2D hole gas in GaAs/(AlGa)As heterostructures, JETP Lett. **67**, 113 (1998).

[5] V. Kravchenko, N. Minina, A. Savino. P. Hansen, C. B. Sorensen, and W. Kraak, Positive magnetoresistance and hole-hole scattering in GaAs/$Al_{0.5}Ga_{0.5}$As heterostructures under uniaxial compression, Phys. Rev. B **59**, 2376 (1999).

[6] E. H. Hwang and S. Das Sarma, Temperature dependent resistivity of spin-split subbands in GaAs two-dimensional hole systems, Phys. Rev. B **67**, 115316 (2003).

[7] E. B. Olshanetsky, Z. D. Kvon, M. V. Entin, L. I. Magarill, N. N. Mikhailov, and S. A. Dvoretsky, Scattering processes in a two-dimensional semimetal, JETP Lett. **89**, 290 (2009).

[8] M. V. Entin, L. I. Magarill, E. B. Olshanetsky, Z. D. Kvon, N. N. Mikhailov, and S. A. Dvoretsky, The effect of electron-hole scattering on transport properties of a 2D semimetal in the HgTe quantum well J. Exp. Theor. Phys. **117**, 933 (2013).

[9] C. Tan, D. Y. H. Ho, L. Wang, J. I. A. Li, I. Yudhistira, D. A. Rhodes, T. Taniguchi, K. Watanabe, K. Shepard, P. L. McEuen *et al.*, Dissipation-enabled hydrodynamic conductivity in a tunable bandgap semiconductor, Sci. Adv. **8**, eabi8481 (2022).

[10] D. A. Bandurin, A. Principi, I. Y. Phinney, T. Taniguchi, K. Watanabe, and P. Jarillo-Herrero, Interlayer electron-hole friction in tunable twisted bilayer graphene semimetal, Phys. Rev. Lett. **129**, 206802 (2022).

[11] G. M. Gusev, A. D. Levin, E. B. Olshanetsky, Z. D. Kvon, V. M. Kovalev, M. V. Entin, and N. N. Mikhailov, Interaction-dominated transport in two-dimensional conductors: From degenerate to partially degenerate regime, Phys. Rev. B **109**, 035302 (2024).

[12] B. Büttner, C. X. Liu, G. Tkachov, E. G. Novik, C. Brne, H. Buhmann, E. M. Hankiewicz, P. Recher, B. Trauzettel, S. C. Zhang *et al.*, Single valley Dirac fermions in zero-gap HgTe quantum wells, Nat. Phys. **7**, 418 (2011).

[13] D. A. Kozlov, Z. D. Kvon, N. N. Mikhailov, and S. A. Dvoretskii, Weak localization of Dirac fermions in HgTe quantum wells, JETP Lett. **96**, 730 (2013).

[14] G. M. Gusev, D. A. Kozlov, A. D. Levin, Z. D. Kvon, N. N. Mikhailov, and S. A. Dvoretsky, Robust helical edge transport at $\nu = 0$ quantum Hall state, Phys. Rev. B **96**, 045304 (2017).

[15] S. S. Krishtopenko, W. Desrat, K. E. Spirin, C. Consejo, S. Ruffenach, F. Gonzalez-Posada, B. Jouault, W. Knap, K. V. Maremyanin, V. I. Gavrilenko *et al.*, Massless Dirac fermions in III-V semiconductor quantum wells, Phys. Rev. B **99**, 121405(R) (2019).

[16] Z. D. Kvon, E. B. Olshanetsky, D. A. Kozlov N. N. Mikhailov, and S. A. Dvoretsky, Two-dimensional electron-hole system in a HgTe-based quantum well, JETP Lett. **87**, 502 (2008).

[17] A. Lucas and S. Das Sarma, Electronic hydrodynamics and the breakdown of the Wiedemann-Franz and Mott laws in interacting metals, Phys. Rev. B **97**, 245128 (2018).

[18] A. Levchenko, S. Li, and A. V. Andreev, Giant magnetoresistance in weakly disordered non-Galilean invariant conductors, Phys. Rev. B **109**, 075401 (2024).

[19] M. Müller, J. Schmalian, and L. Fritz, Graphene: A nearly perfect fluid, Phys. Rev. Lett. **103**, 025301 (2009).

[20] M. König, S. Wiedmann, C. Brune, A. Roth, H. Buhmann, L. W. Molenkamp, X.-L. Qi, and S.-C. Zhang, Quantum spin Hall insulator state in HgTe quantum wells, Science **318**, 766 (2007).

[21] M. Z. Hasan and C. L. Kane, Colloquium: Topological insulators, Rev. Mod. Phys. **82**, 3045 (2010).

[22] Z. D. Kvon, D. A. Kozlov, E. B. Olshanetsky, G. M. Gusev, N. N. Mikhailov, and S. A. Dvoretsky, Topological insulators based on HgTe, Phys. Usp. **63**, 629 (2020).

[23] G. M. Gusev, Z. D. Kvon, E. B. Olshanetsky, N. N. Mikhailov, Mesoscopic transport in two-dimensional topological insulators, Solid State Commun. **302**, 113701 (2019).

[24] L. G. Gerchikov and A. V. Subashiev, Interface states in subband structure of semiconductor quantum wells, Phys. Status Solidi B **160**, 443 (1990).

[25] C. L. Kane and E. J. Mele, $Z_2$ topological order and the quantum spin Hall effect, Phys. Rev. Lett. **95**, 146802 (2005).

[26] B. A. Bernevig and S. C. Zhang, Quantum spin Hall effect, Phys. Rev. Lett. **96**, 106802 (2006).

[27] B. A. Bernevig, T. L. Hughes, and S. C. Zhang, Quantum spin Hall effect and topological phase transition in HgTe quantum wells, Science **314**, 1757 (2006).

[28] S. S. Krishtopenko, and F. Teppe, Quantum spin Hall insulator with a large bandgap, Dirac fermions, and bilayer graphene analog, Sci. Adv. **4**, eaap7529 (2018).

[29] P. Michetti, J. C. Budich, E. G. Novik, and P. Recher, Tunable quantum spin Hall effect in double quantum wells, Phys. Rev. B **85**, 125309 (2012).

[30] G. J. Ferreira, D. R. Candido, F. G. G. Hernandez, G. M. Gusev, E. B. Olshanetsky, N. N. Mikhailov and S. A. Dvoretsky, Engineering topological phases in triple HgTe/CdTe quantum wells, Sci. Rep. **12**, 2617 (2022).

[31] G. M. Gusev, E. B. Olshanetsky, F. G. G. Hernandez, O. E. Raichev, N. N. Mikhailov, and S. A. Dvoretsky, Two-dimensional topological insulator state in double HgTe quantum well, Phys. Rev. B **101**, 241302(R) (2020).

[32] G. M. Gusev, E. B. Olshanetsky, F. G. G. Hernandez, O. E. Raichev, N. N. Mikhailov, and S. A. Dvoretsky, Multiple crossings of Landau levels of two-dimensional fermions in double HgTe quantum wells, Phys. Rev. B **103**, 035302 (2021).

[33] Ye. O. Melezhik, J. V. Gumenjuk-Sichevska, and F. F. Sizov, Electron relaxation and mobility in the inverted band quantum well CdTe/$Hg_{1-x}Cd_xTe$/CdTe, Semicond. Phys. Quantum Electron. Optoelectron. **17**, 85 (2014).

[34] J. Appel and A. W. Overhauser, Cyclotron resonance in two interacting electron systems with application to Si inversion layers, Phys. Rev. B **18**, 758 (1978).

[35] H. Liu and D. Culcer, Coulomb drag in topological materials, J. Phys. Chem. Solids **128**, 54 (2019).

[36] M. Polini and A. K. Geim, Viscous electron fluids, Phys. Today **73**(6), 28 (2020).

[37] Y. Nam, D.-K. Ki, D. Soler-Delgado, and A. F. Morpurgo, Electron-hole collision limited transport in charge-neutral bilayer graphene, Nat. Phys. **13**, 1207 (2017).